

## **Chapter 5:**

# **Modeling and Experimental Validation of**

# **1-D Apertures with Attached Piezoelectric Material**

## **5.1 Introduction**

Keeping the ultimate goal of designing ultra-large membrane optics and radar apertures in mind, one of the key research areas that needs to be addressed is understanding the dominant physics of such structures. In this chapter, we will model a strip sample of Kapton material with a PZT bimorph bonded to one end. In doing so, we will create a 1-D model of the more complex 2-D structure. We will be able to use the developed 1-D model to capture the underlying physics of the augmented system. In this chapter, we will first outline the procedure for putting the beam under axial loading dynamic equation into weak form. This will enable us to approximate the system dynamics using the finite element method and cubic B-splines. Then, we will validate our developed model against experimental data. Next, we will define the LQR control problem and show through simulation that the 1-D sample can be controlled using the bonded PZT bimorph. Finally, we will discuss the formulation for the functional gains of the 1-D system.

## **5.2 Constructing the Finite Element Matrices for the 1-D Beam Under Axial Loading System**

This section steps through the derivation of the weak form governing the transverse dynamics of a beam under axial loading. It begins with the dynamics of the undamped system, and systematically adds in the effects of viscous air damping, internal visco-elastic Kelvin-Voigt damping, and also the distributed moment generated by the PZT bimorph actuator. This 1-D model will then be verified through experimental dynamic analysis of a Kapton – PZT bimorph system.

### 5.2.1 Derivation of the Weak Form for the 1-D Membrane / PZT System

Given the transverse vibration dynamical equation of a beam under axial loading, namely,

$$\frac{\partial^2}{\partial x^2} \left[ E(x)I(x) \frac{\partial^2 w(x,t)}{\partial x^2} \right] - \frac{\partial}{\partial x} \left[ P(x) \frac{\partial w(x,t)}{\partial x} \right] + \rho(x)A(x) \frac{\partial^2 w(x,t)}{\partial t^2} = 0, \quad (5.1)$$

we wish to derive the weak form of these dynamics for the purpose of applying finite elements to create a system model. In Equation 5.1, the sign convention of  $P(x)$  is positive if the applied axial load is tensile and negative if the applied axial load is compressive. As stated previously,  $E(x)$  is the elastic modulus,  $I(x)$  is the area moment of inertia,  $\rho(x)$  is the density, and  $A(x)$  is the cross-sectional area of the beam.

First, we assume that the system consists of two states, position and velocity, or  $w(x,t)$  and  $v(x,t)$ , respectively. Then we can write two equations,

$$w_t(x,t) = v(x,t) \quad (5.2a)$$

$$\rho(x)A(x)v_t(x,t) = -[E(x)I(x)w_{xx}(x,t)]_{xx} + [P(x)w_x(x,t)]_x. \quad (5.2b)$$

Now we will multiply through both Equations 5.2a and 5.2b by test functions  $\phi(x)$  and  $\psi(x)$ , respectively, and then integrate the equations over the span of the structure. Doing so yields the equations:

$$\frac{\partial}{\partial t} \int_0^L w(x,t)\phi(x) dx = \int_0^L v(x,t)\phi(x) dx \quad (5.3a)$$

$$\frac{\partial}{\partial t} \int_0^L \rho(x) A(x) v(x, t) \psi(x) dx = - \int_0^L [E(x) I(x) w_{xx}(x, t)]_{xx} \psi(x) dx + \int_0^L [P(x) w_x(x, t)]_x \psi(x) dx \quad (5.3b)$$

Next, we integrate Equation 5.3b by parts twice. Doing so yields:

$$\begin{aligned} \frac{\partial}{\partial t} \int_0^L \rho(x) A(x) v(x, t) \psi(x) dx &= - \int_0^L [E(x) I(x) w_{xx}(x, t)] \psi_{xx}(x) dx - \int_0^L [P(x) w_x(x, t)] \psi_x(x) dx \\ &\quad + [E(x) I(x) w_{xx}(x, t) \psi_x(x)]_0^L - [E(x) I(x) w_{xx}(x, t)]_x \psi(x) \Big|_0^L \\ &\quad + [P(x) w_x(x, t)] \psi(x) \Big|_0^L . \end{aligned} \quad (5.4)$$

For the system we are trying to model, we will assume that the boundary conditions are pinned-pinned. We are assuming pinned-pinned as such a boundary condition can be tested in the laboratory. Physically, a pinned end cannot translate in any direction and also cannot sustain a bending moment. Mathematically speaking, these conditions are imposed through the following boundary conditions:

$$w(0, t) = w(L, t) = 0 , \quad (5.5a)$$

$$E(0) I(0) w_{xx}(0, t) = E(L) I(L) w_{xx}(L, t) = 0 , \quad (5.5b)$$

$$v(0, t) = v(L, t) = 0 . \quad (5.5c)$$

Now, we wish to enforce the boundary conditions, Equations 5.5, in Equation 5.4. Notice that the first boundary term of Equation 5.4 vanishes because of the natural boundary conditions imposed by Equation 5.5b, and, by forcing

$$\psi(0) = \psi(L) = 0 , \quad (5.6)$$

the second and third boundary terms in Equation 5.4 also vanish. It is natural when using the finite element method to require the test functions to match the same geometric boundary conditions as the unknown functions, as shown in Equations 5.6 and 5.5a (Fix and Strang, 1973). Hence, we arrive at the weak form of Equation 5.4, given by

$$\frac{\partial}{\partial t} \int_0^L \rho(x) A(x) v(x, t) \psi(x) dx = - \int_0^L [E(x) I(x) w_{xx}(x, t)] \psi_{xx}(x) dx - \int_0^L [P(x) w_x(x, t)] \psi_x(x) dx . \quad (5.7)$$

Next, we wish to approximate the dynamics given by Equations 5.3a and 5.7. To do so, we let

$$\begin{aligned} w(x, t) &= \sum_{i=1}^N w_i(t) \phi_i(x) \\ v(x, t) &= \sum_{i=1}^N v_i(t) \phi_i(x) \end{aligned} \quad (5.8)$$

Note that the test functions introduced in Equations 5.3 were dummy functions yet to be determined, and therefore, since they live in the same Hilbert space  $H^2(0, L) \cap H_0^1(0, L)$ , we can let  $\varphi(x) = \psi(x)$ . In other words, the test functions are required to satisfy the same boundary conditions (as shown in Equations 5.5a and 5.5c), so they can be taken from the same functional space. Plugging in our approximations (Equations 5.8) into Equations 5.3a and 5.7 yields:

$$\frac{\partial}{\partial t} \sum_{i=1}^N w_i \int_0^L \phi_i \phi_j dx = \sum_{i=1}^N v_i \int_0^L \phi_i \phi_j dx \quad (5.9a)$$

$$\frac{\partial}{\partial t} \sum_{i=1}^N v_i \int_0^L \rho A \phi_i \phi_j dx = - \sum_{i=1}^N w_i \int_0^L P(\phi_i)_x (\phi_j)_x dx - \sum_{i=1}^N w_i \int_0^L EI(\phi_i)_{xx} (\phi_j)_{xx} dx . \quad (5.9b)$$

By letting

$$\begin{aligned}
M_1 &= \left[ \int_0^L \phi_i \phi_j dx \right]_{i,j=1}^N \\
M_2 &= \left[ \int_0^L \rho A \phi_i \phi_j dx \right]_{i,j=1}^N \\
A_{11} &= \left[ \int_0^L P(\phi_i)_x (\phi_j)_x dx \right]_{i,j=1}^N \\
A_{22} &= \left[ \int_0^L EI(\phi_i)_{xx} (\phi_j)_{xx} dx \right]_{i,j=1}^N
\end{aligned} \tag{5.10}$$

We arrive at the finite element matrix form of the dynamic equations governing the transverse vibration of the system,

$$\begin{bmatrix} M_1 & 0 \\ 0 & M_2 \end{bmatrix} \begin{bmatrix} \bar{w} \\ \bar{v} \end{bmatrix}_t = \begin{bmatrix} 0 & M_1 \\ -[A_{11} + A_{22}] & 0 \end{bmatrix} \begin{bmatrix} \bar{w} \\ \bar{v} \end{bmatrix}. \tag{5.11}$$

### 5.2.2 Addition of Viscous Air Damping and Kelvin-Voigt Damping

Next, we would like to add terms to represent damping imposed by an external fluid medium (like air) and internal damping. To do this, we augment the system dynamics in Equation 5.1:

$$\begin{aligned}
&\frac{\partial^2}{\partial x^2} \left[ E(x)I(x) \frac{\partial^2 w(x,t)}{\partial x^2} \right] - \frac{\partial}{\partial x} \left[ P(x) \frac{\partial w(x,t)}{\partial x} \right] + \rho(x)A(x) \frac{\partial^2 w(x,t)}{\partial t^2} \\
&+ \gamma \frac{\partial w(x,t)}{\partial t} + \frac{\partial^2}{\partial x^2} \left[ \beta(x)I(x) \frac{\partial^3 w(x,t)}{\partial x^2 \partial t} \right] = 0
\end{aligned} \tag{5.12}$$

The constant term  $\gamma$  is based on the external fluid medium, whereas the term  $\beta(x)$  represents the energy dissipation by friction internal to the beam. Now we will focus on Equation 5.12, as Equations 5.2a, 5.3a, and 5.9a do not change through the introduction of the damping terms. Following the same procedure as previously outlined, we have:

$$\begin{aligned} \rho(x)A(x)v_t(x,t) = & -[E(x)I(x)w_{xx}(x,t)]_{xx} + [P(x)w_x(x,t)]_x \dots \\ & - \gamma v(x,t) - [\beta(x)I(x)v_{xx}(x,t)]_{xx} . \end{aligned} \quad (5.13)$$

Multiplying through by our test functions and integrating yields:

$$\begin{aligned} \frac{\partial}{\partial t} \int_0^L \rho(x)A(x)v(x,t)\psi(x) dx = & -\int_0^L [E(x)I(x)w_{xx}(x,t)] \psi_{xx}(x) dx - \int_0^L [P(x)w_x(x,t)] \psi_x(x) dx \\ & + [E(x)I(x)w_{xx}(x,t)\psi_x(x)]_0^L - [E(x)I(x)w_{xx}(x,t)]_x \psi(x) \Big|_0^L \\ & + [P(x)w_x(x,t)] \psi(x) \Big|_0^L - [\beta(x)I(x)v_{xx}(x,t)]_x \psi(x) \Big|_0^L \\ & + [\beta(x)I(x)v_{xx}(x,t)] \psi_x(x) \Big|_0^L - \int_0^L [\beta(x)I(x)v_{xx}(x,t)] \psi_{xx}(x) dx \\ & - \gamma \int_0^L v(x,t)\psi(x) dx \end{aligned} \quad (5.14)$$

Again, we enforce natural boundary conditions and the geometric boundary conditions from the pinned-pinned beam geometry by setting

$$\psi(0) = \psi(L) = 0 . \quad (5.15)$$

Doing so yields the weak form of Equation 5.13:

$$\begin{aligned} \frac{\partial}{\partial t} \int_0^L \rho(x)A(x)v(x,t)\psi(x) dx = & -\int_0^L [E(x)I(x)w_{xx}(x,t)] \psi_{xx}(x) dx - \int_0^L [P(x)w_x(x,t)] \psi_x(x) dx \\ & - \int_0^L [\beta(x)I(x)v_{xx}(x,t)] \psi_{xx}(x) dx - \gamma \int_0^L v(x,t)\psi(x) dx \end{aligned} \quad (5.16)$$

Plugging in our approximations (Equations 5.8), and by letting:

$$D_1 = \left[ \int_0^L \beta I(\psi_i)_{xx} (\psi_j)_{xx} dx \right]_{i,j=1}^N , \quad (5.17)$$

we can write our approximate system dynamics in matrix form, namely:

$$\begin{bmatrix} M_1 & 0 \\ 0 & M_2 \end{bmatrix} \begin{bmatrix} \bar{w} \\ \bar{v} \end{bmatrix}_t = \begin{bmatrix} 0 & M_1 \\ -[A_{11} + A_{22}] & -\gamma M_1 - D_1 \end{bmatrix} \begin{bmatrix} \bar{w} \\ \bar{v} \end{bmatrix}. \quad (5.18)$$

### 5.2.3 Constructing the Input Matrix for Actuating the PZT Bimorph

Having constructed the state matrix (Equation 5.18) to capture the localized mass and stiffness contributions from the attached piezoelectric bimorph, we now wish to formulate the input matrix,  $B$ , to model using the bimorph to generate a distributed moment in our control system design. The piezoelectric bimorph produces an external moment which can be written as:

$$M_{pzt} = \frac{1}{2} E_{pzt} d_{31} (h + h_{pzt}) [V_1(t) - V_2(t)], \quad (5.19)$$

where  $E_{pzt}$  is the modulus of the piezoelectric patch,  $d_{31}$  is the electromechanical coupling coefficient,  $h$  is the thickness of the substrate,  $h_{pzt}$  is the thickness of the piezoelectric patch, and  $V_1$  and  $V_2$  are the applied control voltages sent to *patch 1* and *patch 2* of the bimorph, respectively. In a bimorph configuration, it is important to note that the voltages sent to each patch are equal but opposite in sign to generate a pure bending moment. The derivation of Equation 5.19 is extensively covered by Banks, Smith, and Wang (1996). A review of this derivation is as follows.

Given a piezoelectric bimorph bonded to a flat structure (as shown in Figure 5.1), the magnitude of the strain induced by the actuators is given by:

$$\left( \varepsilon_{pzt} \right)_i = \frac{d_{31}}{h_{pzt}} V_i(t), \quad (5.20)$$

where the subscript  $i$  denotes either *patch 1* or *patch 2*. The induced strain is then assumed to be directly proportional to the modulus of the piezoelectric patch, namely,

$$(\sigma_{pz})_i = E_{pz} \varepsilon_{pz} = E_{pz} \frac{d_{31}}{h_{pz}} V_i(t). \quad (5.21)$$

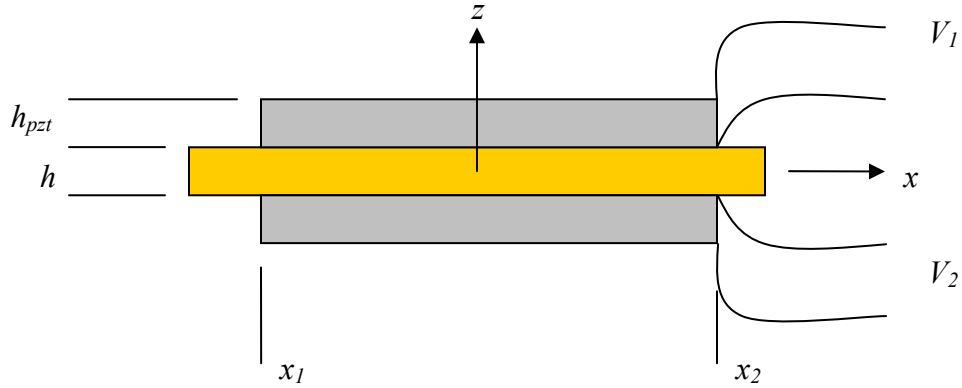


**Figure 5.1.** Cross-sectional area of the piezoelectric bimorph attached to the membrane film.

To get the external moment resultant, we need to integrate Equation 5.21 over the face of the element through the thickness of the combined structure. Doing so yields

$$M_{pz1} = \int_{h/2}^{h/2+h_{pz}} \sigma_{pz} z dz = \frac{1}{2} E_{pz} \frac{d_{31}}{h_{pz}} \left[ \left( \frac{1}{2} h + h_{pz} \right)^2 - \left( \frac{1}{2} h \right)^2 \right] V_1(t). \quad (5.22)$$

Equation 5.22 is the moment resultant from just a single patch. Similar analysis for the other patch in the bimorph pair results in an equivalent moment resultant but with opposite sign. For simplicity, we can rewrite Equation 5.22 as

$$M_{pz1} = K_B V_1(t), \quad (5.23)$$

where, after simplification,

$$K_B = \frac{1}{2} E_{pzt} \frac{d_{31}}{h_{pzt}} \left[ \left( \frac{1}{2} h + h_{pzt} \right)^2 - \left( \frac{1}{2} h \right)^2 \right] = \frac{1}{2} E_{pzt} d_{31} (h + h_{pzt}). \quad (5.24)$$

Consequently, the resulting moment generated by the bimorph can be written as

$$M_{pzt} = K_B [V_1(t) - V_2(t)]. \quad (5.25)$$

Until now, we haven't taken into account the fact that the bimorph has finite length along the sample's surface (given by locations  $x_1$  and  $x_2$  along the span of the structure). The discontinuity can be incorporated using a  $\chi(x)$  indicator function (following the notation of Banks, Smith, and Wang, 1996), where

$$\chi(x) = \begin{cases} 1 & \text{if } x_1 \leq x \leq x_2 \\ 0 & \text{otherwise} \end{cases}, \quad (5.26)$$

thus giving us

$$M_{pzt} = K_B [V_1(t) - V_2(t)] \chi(x). \quad (5.27)$$

Equation 5.27 enters into our equation of motion in the form of a distributed moment with units of  $\frac{N \cdot m}{m}$ , and performing a moment balance on a differential element, it appears as:

$$\frac{\partial^2}{\partial x^2} (bM_{pzt}), \quad (5.28)$$

where  $b$  is the width of the patch. Equation 5.28 can also be placed into the weak form through integration by parts, and doing so yields

$$\int_0^L \left[ \frac{\partial^2}{\partial x^2} bM_{pzt} \right] \psi \, dx = \int_0^L bM_{pzt} \psi_{,xx} \, dx. \quad (5.29)$$

Again, the boundary terms from our integration by parts have been eliminated because of the boundary conditions of the problem. Since we have put the distributed moment into the weak form, we can now combine Equation 5.29 with our system dynamics given by Equation 5.18. Thus, we arrive at the approximated weak form of our augmented system, including the control effect of the piezoelectric bimorph, namely,

$$\begin{bmatrix} M_1 & 0 \\ 0 & M_2 \end{bmatrix} \begin{bmatrix} \bar{w} \\ \bar{v} \end{bmatrix}_t = \begin{bmatrix} 0 & M_1 \\ [A_{11} - A_{22}] & -\gamma M_1 - D_1 \end{bmatrix} \begin{bmatrix} \bar{w} \\ \bar{v} \end{bmatrix} + Bu(t), \quad (5.30)$$

where

$$B = \begin{bmatrix} 0 \\ \tilde{b} \end{bmatrix}, \quad (5.31)$$

and where, after our integration by parts,

$$\tilde{b} = \left[ \int_0^L bM_{pzt} (\phi_i)_{,xx} \, dx \right]_{i=1}^N. \quad (5.32)$$

### 5.3 Experimental Validation of the Finite Element Model

Equation 5.18 is the finite element approximation to the system dynamics governing the transverse vibrations of a beam under axial loading and includes viscous effects from both the surrounding medium, like air, and internal damping from the Kelvin-Voigt damping model. We now desire to validate the developed model, Equation 5.30, by designing an experiment that captures the dynamic effects of a membrane strip under a tensile load with an augmented piezoelectric patch.

### 5.3.1 Experimental Hardware and Test Setup

The experimental setup consists of a 21.8 x 1.8 cm strip sample of Kapton HN (51  $\mu\text{m}$  thick). Two wafers of H4 piezoelectric material (3.6 cm in length) were glued to the membrane sample to serve as the excitation actuator for the system. Copper tape was used as the conductive layer on one side of the H4 PZT wafer to attach one lead wire, and a second lead wire was attached to the opposite side of the PZT wafer using SuperSafe Superior #30 Soft Solder Flux Liquid. A diagram of the membrane sample with attached PZT is shown below in Figure 5.2. Table 5.1 describes the relevant material properties of the Kapton and H4 PZT wafer.

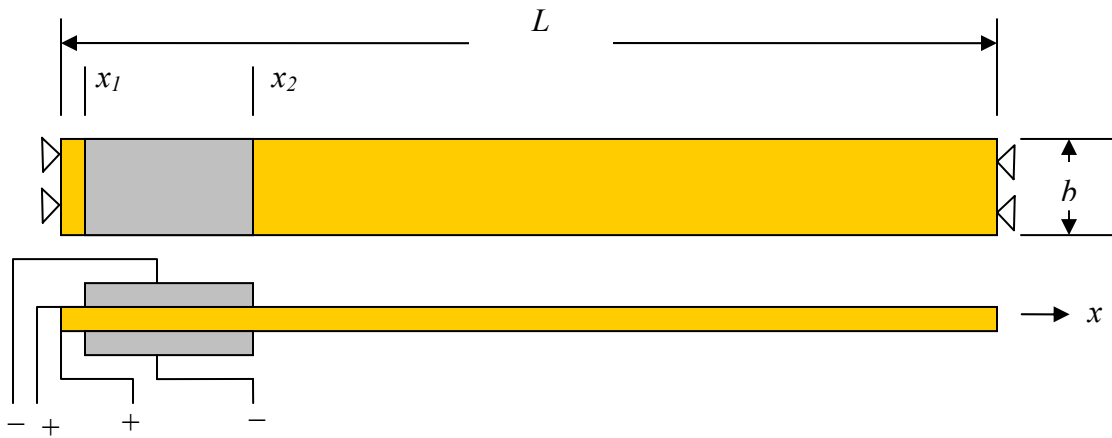


**Figure 5.2.** Diagram of the Kapton HN sample with attached PZT bimorph, including top view (above) and side view (below).

**Table 5.1.** Relevant material properties for Kapton HN and H4 PZT.

	Parameter	Symbol	Value
Kapton HN	modulus	$E$	165 MPa
	length	$L$	21.8 cm
	width	$b$	1.8 cm
	thickness	$t$	51 $\mu\text{m}$
	density	$\rho$	1400 $\text{kg/m}^3$
	viscous air damping	$\gamma$	0.02
	Poisson's ratio	$\nu$	0.34
	shear modulus	$G$	86.2 MPa
	H4 PZT Wafer	coupling coefficient	$d_{31}$
modulus		$E_{pzt}$	62 GPa
patch length		$L_{pzt}$	3.6 cm
patch width		$b_{pzt}$	1.9 cm
patch thickness		$t_{pzt}$	533.4 $\mu\text{m}$
density		$\rho_{pzt}$	7800 $\text{kg/m}^3$
Poisson's ratio		$\nu_{pzt}$	0.31
shear modulus		$G_{pzt}$	2.36 GPa

The Kapton HN sample was held in place by two grippers. Each gripper has two aluminum rods pushed through two opposing channels and are held in place by an interference fit. The rods serve as the contact points to hold the sample in place, and thus form pinned-pinned boundary conditions. The grippers are aligned by bolting them to a frame made of extruded aluminum stock (80/20 series 1515). While one gripper is held permanently in place, the other gripper is attached to a lead screw for easy travel in the  $x$ -direction along the axis of the membrane sample. This allows for uniform tensile loads to be applied to the sample. The tensile load applied to the membrane sample is measured by a Transducer Techniques load cell (model #MLP-75). The load cell output is measured by an Omegadyne strain gage meter (model #LC101-50). A picture of the experimental setup, including the H4 PZT bimorph, grippers, and load cell, is shown in Figure 5.3.

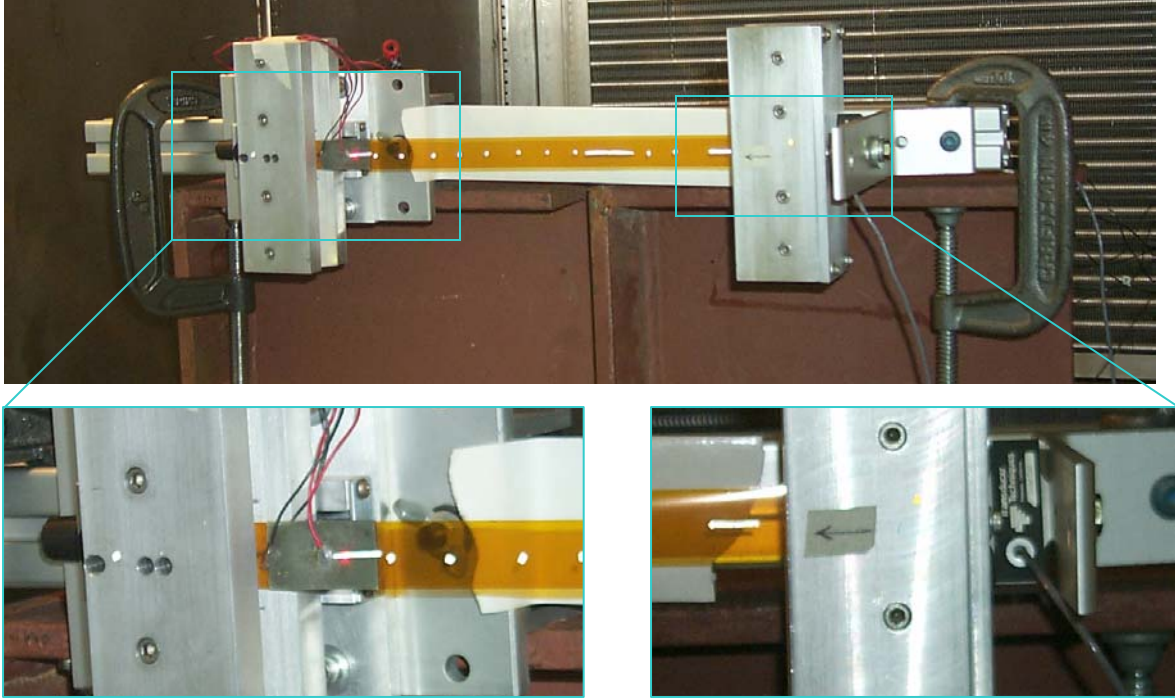


**Figure 5.3.** Photograph of the experimental setup showing the Kapton membrane held under tension (top), with close-up photos of the PZT bimorph (bottom left) and Transducer Techniques load cell (bottom right). In this picture, the left gripper is attached to the lead screw.

The entire experimental setup was housed in an environmental vacuum chamber (Tenney Environmental Model 36 ST SN27429). The chamber served two purposes. Firstly, while testing in ambient conditions, the chamber served as an excellent shield from external vibratory disturbances, such as air conditioning currents. Secondly, a series of tests could be run at near-vacuum to eliminate the effect of ambient air pressure around the test specimen. The response of the membrane sample was measured using a Polytec laser vibrometer (laser head #OFV 303 and control signal box #OFV 3001). The laser vibrometer shines a laser onto the sample and measures either the displacement or velocity (depending on which output channel is selected) of the structure at that particular point through interferometry. The laser vibrometer was selected as the sensor for measuring the response of the system as the mass loading effect from a more traditional accelerometer would have been significant considering the ultra-thin nature of the Kapton

sample. A photo of the test setup, including the vacuum chamber and laser vibrometer, is shown in Figure 5.4. Figure 5.5 presents a schematic of the entire testing setup, including necessary signal conditioning electronics.



**Figure 5.4.** Photograph of the test setup, highlighting the laser vibrometer sensor and the Kapton sample test rig sitting inside of the Tenney Environmental vacuum chamber.

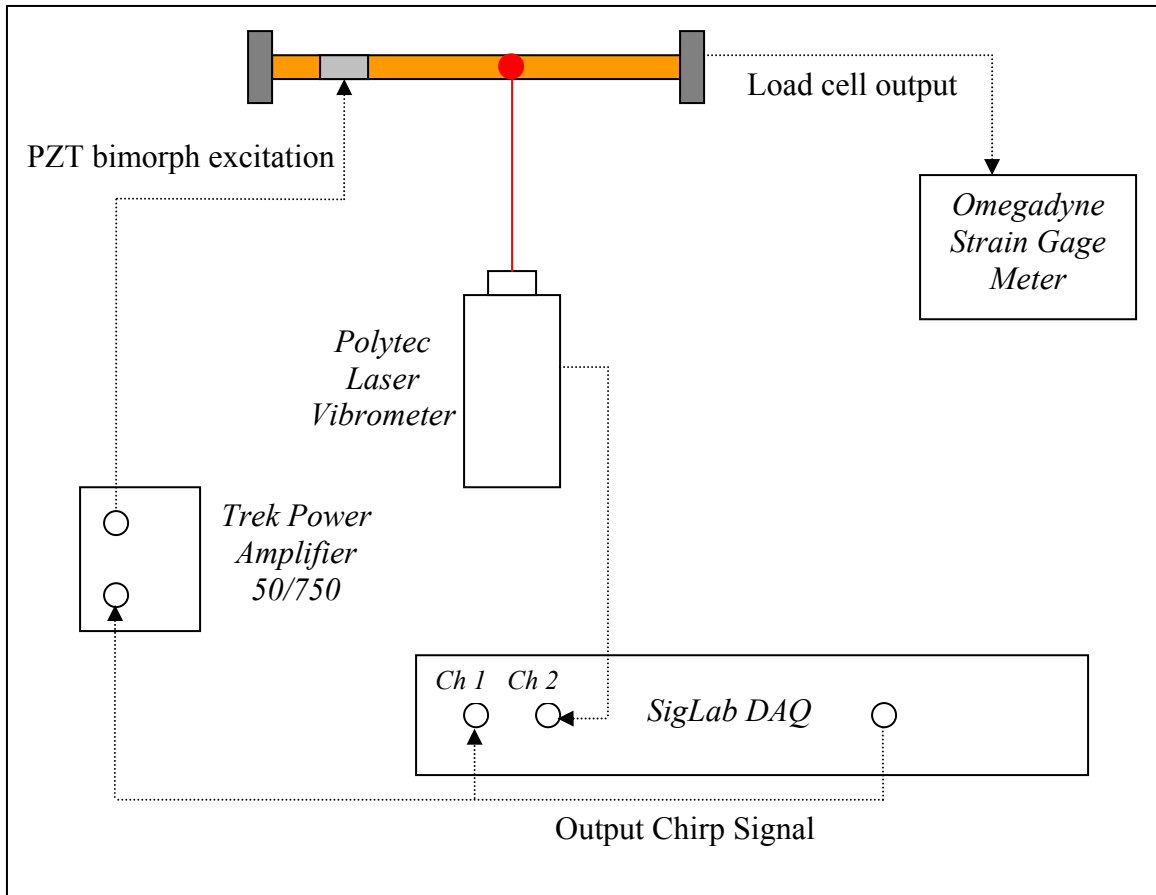


**Figure 5.5.** Schematic of the experimental testing setup to capture the dynamic response of the Kapton sample.

### 5.3.2 Data Acquisition

The excitation signal was generated via MatLab's SigLab Data Acquisition board to excite the attached PZT bimorph. SigLab interfaces through a SCSI card with a PC system and provides a relatively inexpensive means for performing dynamic system analysis. Using SigLab's VNA and VFG toolkits, a burst chirp signal with peak amplitude of 1.0 V and with frequency content ranging from 10 – 500 Hz was generated to excite the PZT bimorph. The burst chirp signal was amplified by a factor of 20 through a Trek Amplifier (model 50/750). The velocity response of the structure was measured using the laser vibrometer at twenty points along the centerline of the membrane strip, one point at a time. The velocity signal was then fed back to input Channel 2 on the SigLab DAQ board. Transfer functions were measured at each of the twenty centerline points along the length of the Kapton sample. Each point was

designated with a small, square piece of highly-reflective tape to help eliminate detrimental backscatter from the laser, consequently improving the quality of the measured signal.

Two sets of tests were initially performed. The first test was run under vacuum conditions, while the second set of tests was run at ambient conditions.

### **5.3.3 Vacuum Test Results**

The vacuum tests were purposefully run prior to any ambient tests. The reason for this is that the membrane sample is subject to out-gassing, and consequently, the tension applied to the specimen would increase while at vacuum. Dupont has documented that out-gassing of primarily carbon monoxide and carbon dioxide occurs in Kapton at vacuum (Dupont Technical Bulletin H-78317, 2002). For this particular experiment, the tensile load increased 5% while transitioning from the ambient pressure equilibrium tension to the vacuum equilibrium tension. All tensile tests in this section were run at 14.3 N.

The Tenney Environmental chamber was set to 10 Torr and 23°C (room temperature). It took the chamber approximately 30 minutes to achieve near-vacuum conditions. The measured velocity response of the membrane at twenty locations is shown in Figure 5.6. The measurement locations correspond to the following distances measured from the left pinned boundary condition (see Figures 5.2 and 5.3 for reference): 1.8, 2.4, 3.3, 4.4, 5.0, 5.4, 6.2, 7.3, 8.4, 9.7, 10.5, 11.6, 12.5, 13.5, 14.6, 15.9, 16.8, 17.8, 18.6, and 19.7 cm.

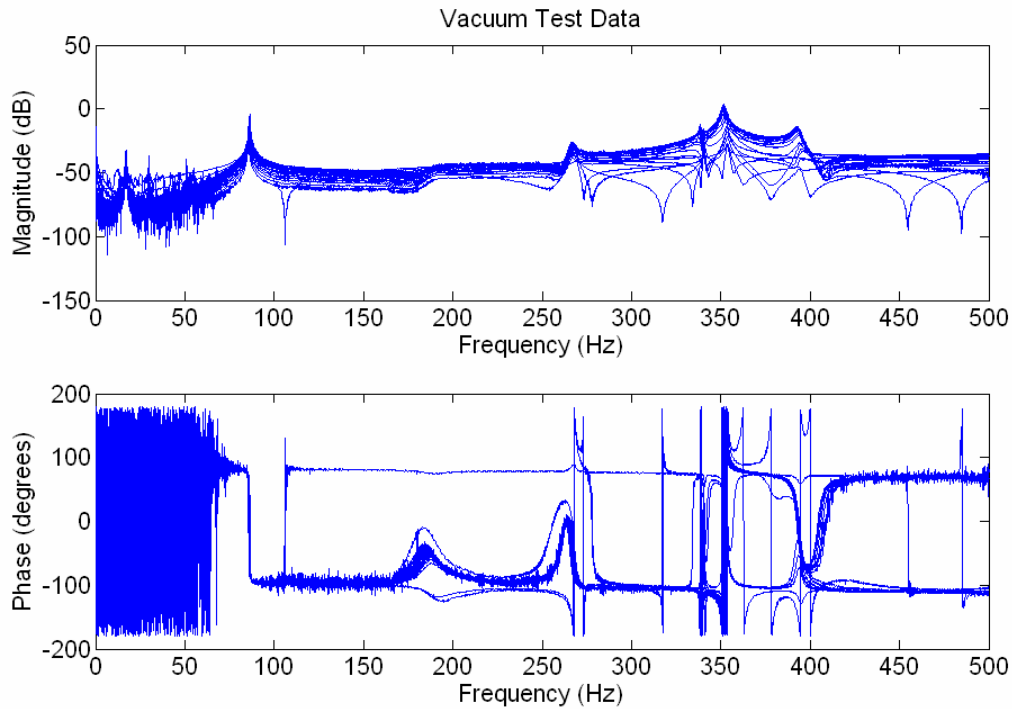


**Figure 5.6.** Bode plot of the membrane structure’s response to the PZT bimorph excitation as measured by a laser vibrometer at 20 distinct locations under vacuum conditions.

The frequency response functions measured along the length of the sample identified resonant frequencies at 86, 267, 339, 352, and 393 Hz. Next, the same test was run but at ambient conditions.

### 5.3.4 Ambient Test Results

Using a test set up identical to the one described in the previous section, the frequency response functions of the membrane sample were generated at the same centerline points as the vacuum tests. However, in contrast to the vacuum tests, the vacuum chamber door was opened to eliminate the need of shining the laser through the front window pane. The tension of the specimen was not disturbed from its position during the vacuum testing. The frequency response of the sample at each of the measured locations is given in Figure 5.7.

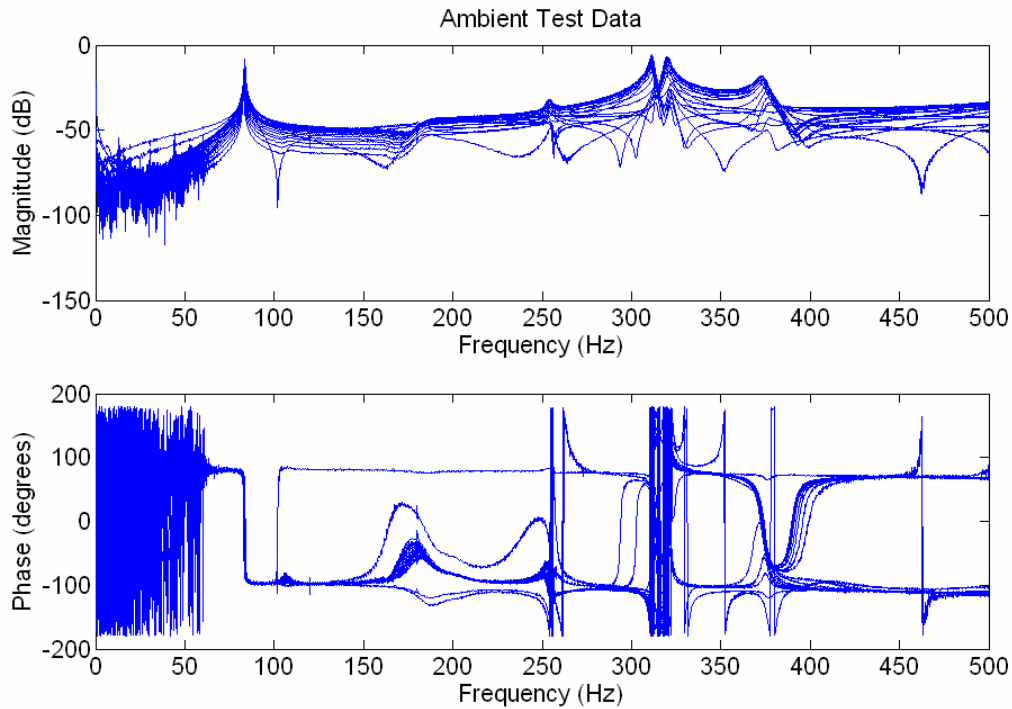


**Figure 5.7.** Bode plot of the membrane structure’s response to the PZT bimorph excitation as measured by a laser vibrometer at 20 distinct locations under ambient conditions.

Under ambient conditions, the dynamic response data indicated resonant frequencies at 83, 254, 311, 321, and 392 Hz. The differences between the two test cases require additional analysis, as provided in the following section.

### 5.3.5 Comparison between Vacuum and Ambient Test Results

A comparison between the measured response of the structure in ambient and vacuum conditions is shown in Figure 5.8. Firstly, a modal analysis of the five resonant peaks found in the 0 – 500 Hz bandwidth was performed. As a result of the analysis, it was determined that both the third and fifth peaks showing up in the vacuum and ambient cases are actually torsional modes of the structure (occurring at 339 and 393 Hz for the vacuum case and 311 and 392 Hz for the ambient case). Frequency response measurements taken off-axis from the centerline demonstrated this torsional behavior. The transverse vibration mode shapes of the structure, as experimentally determined, are

shown in Figure 5.9. For now, our analysis will ignore the torsional modes of the structure, but when we extend our analysis into 2-D using thin plate theory in subsequent chapters, the coupling between the  $x$  and  $y$  coordinates will be included.

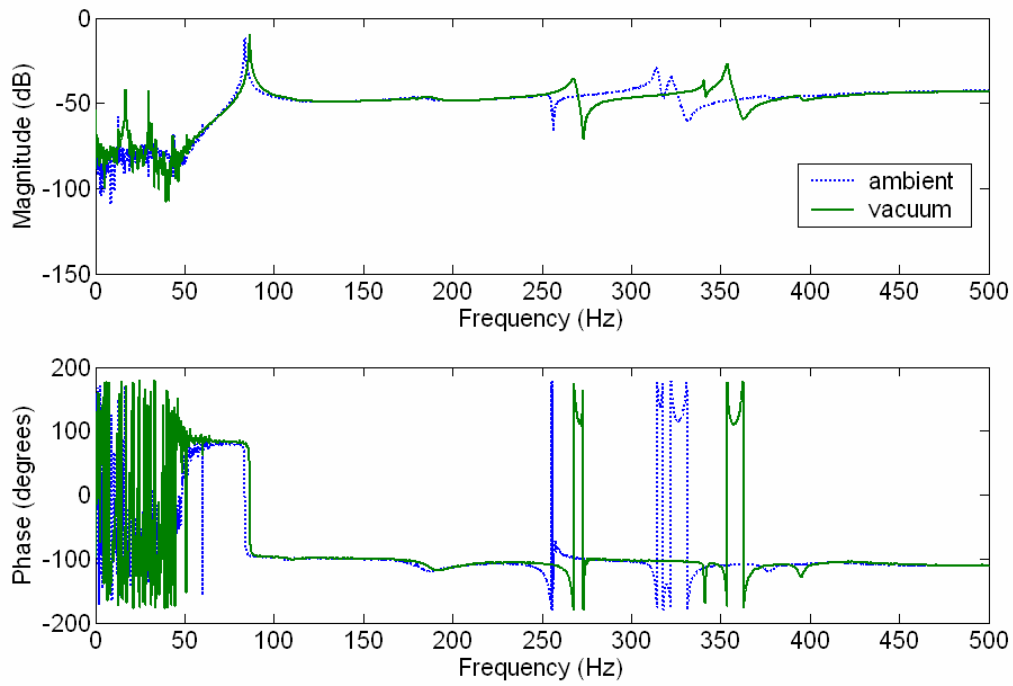


**Figure 5.8.** Vacuum and ambient transfer functions measured 9.7 cm from the left boundary.

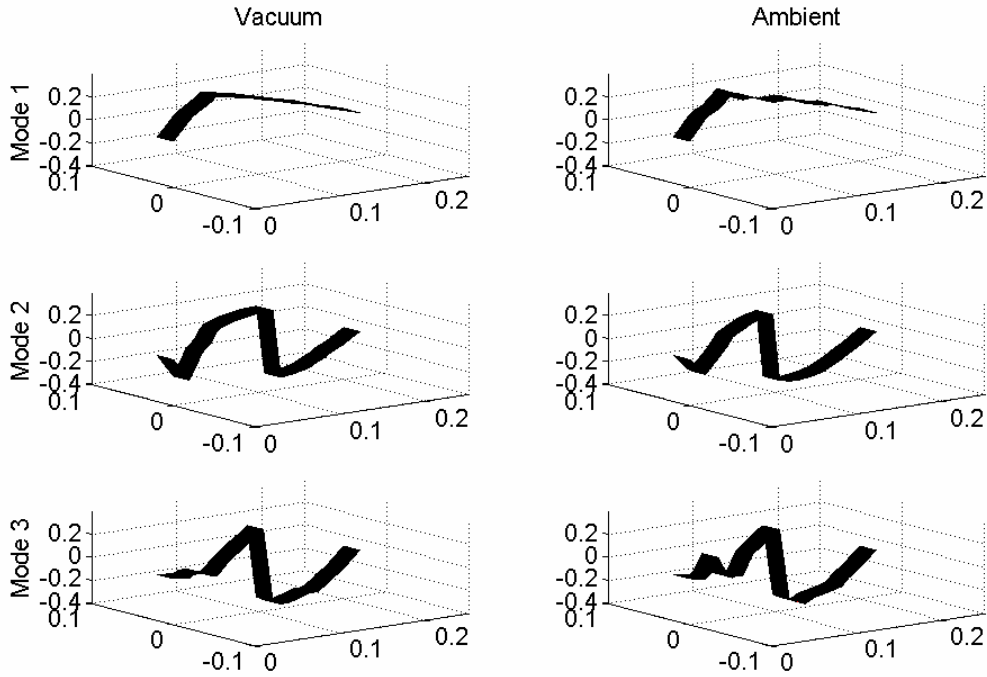


**Figure 5.9.** Experimentally determined transverse vibration mode shapes as measured under vacuum and ambient conditions.

Secondly, we also note that the resonant frequencies (in Figure 5.8) demonstrate an offset between the vacuum and ambient data. The offset of the resonant frequencies is a consequence of two phenomena: out-gassing experienced by the Kapton sample and mass loading from the surrounding air in the chamber. Since the boundaries of the structure are mechanically fixed at the pinned ends, the tensile load experienced by the Kapton sample increases as the material out-gasses (and consequently loses mass). As reported in the Dupont Technical Bulletin (H-78317, 2002), their vacuum tests at high temperature demonstrated a 34.6% weight loss of the Kapton sample as compared to the original sample. Although the test sample from these tests was not exposed to high temperatures, a 10 – 20% change in the density of the structure (as a result of the Kapton losing mass to out-gassing) would produce notable changes in the frequencies of the system. Secondly, air mass loading effects have been documented to be significant for membranous structures (see, for example, Kukathasan and Pellegrino, 2002). The out-gassing phenomenon and mass loading assertions will be explored with our developed finite element model in subsequent sections.

In the next section, we will first establish the validity of the developed finite element model as compared to the measured data, and then use the finite element to understand the effects of mass, both from adding additional actuator material to the system and from losing mass to out-gassing, on the dynamics of the Kapton-PZT strip.

#### **5.4 Finite Element Model Verification**

The next goal is to model the response of the structure using the distributed parameter systems approach as outlined previously in this chapter. First, we will compare the predicted response of the membrane – PZT structure to the actual measured response from the experimental data. Then, we will compare the mode shapes between the two. Finally, we will discuss the applicability of the proposed beam under tension model over a variety of tensile loads and compare the modeled results to actual experimental data.

##### **5.4.1 Transfer Function and Mode Shape Comparison**

Starting with the parameters listed in Table 1, a finite element model using cubic B-splines and 256 elements was built and solved to simulate the expected transfer function of the Kapton membrane. With this first iteration, the resulting frequencies as compared between the FE model and the measured data response were in good agreement. The first three resonant frequencies were simulated to within 1%, 6%, and 2%, respectively. The FE model results and measured results are shown in Figure 5.10.

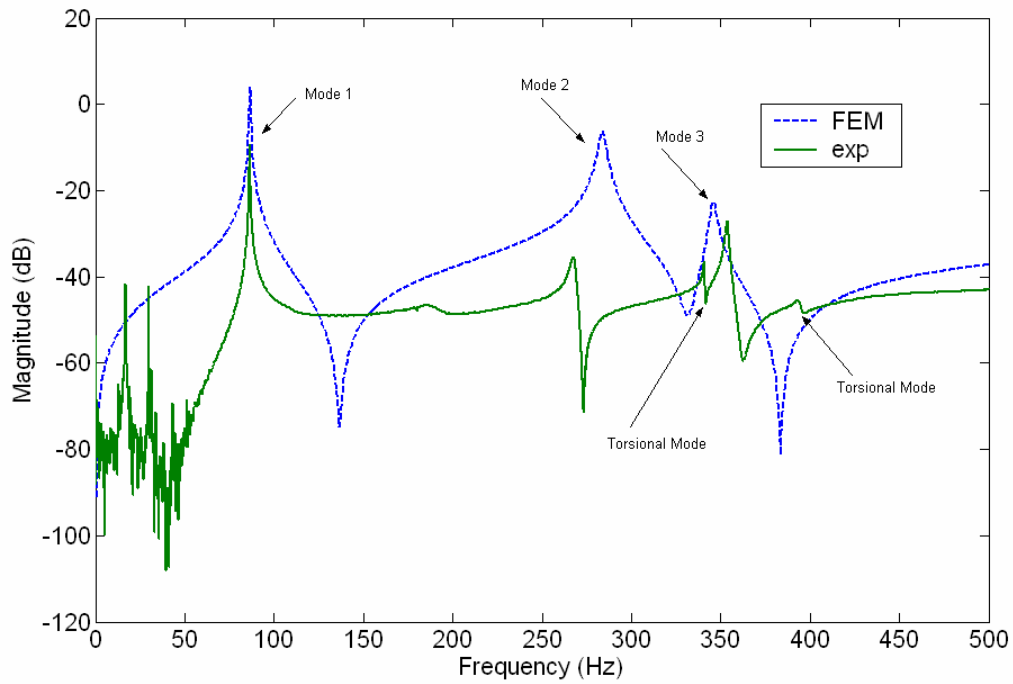


**Figure 5.10.** Comparison between the FE model transfer function (dotted line) and the experimentally determined transfer function (solid line) as measured 2.4 cm from the left boundary condition.

We also can compare the experimentally determined operational mode shapes of the structure to the finite element model predicted mode shapes. Figure 5.11 demonstrates the similarity between the two for the case of vacuum testing.

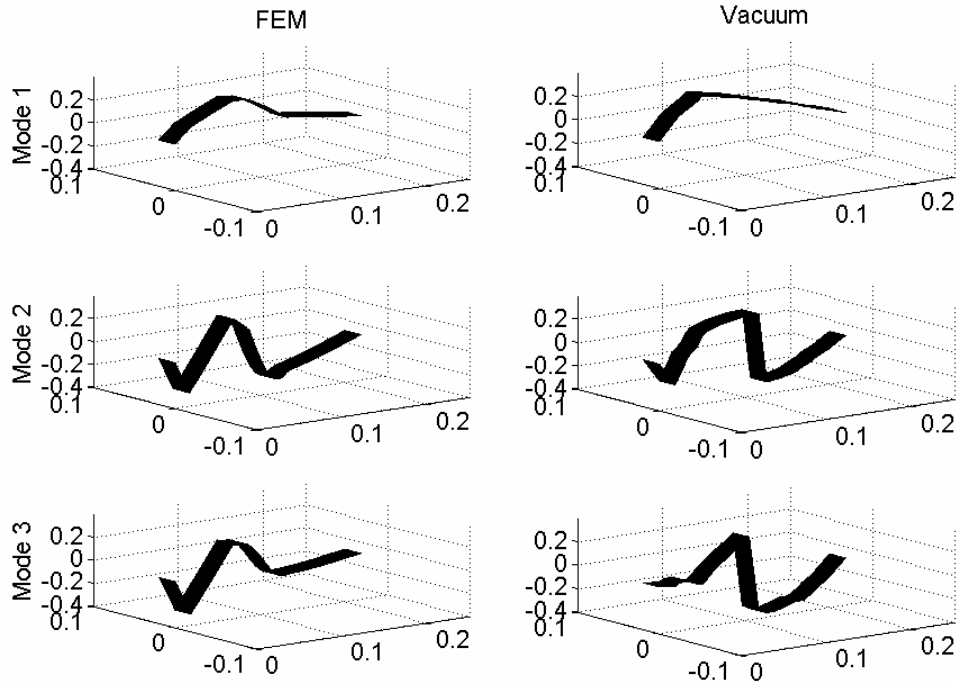


**Figure 5.11.** A comparison between the predicted FE mode shapes (left column) and the experimentally measured mode shapes (right column).

As shown by Figure 5.11, the developed model performs well in predicting the response of the structure. To reiterate, the experimental data contains two torsional modes due to improper mounting of the test specimen during testing and also caused by lack of homogeneity between the two PZT wafers, which would induce a twisting moment into the structure. Although the current model does not address the coupling between the torsional and transverse modes of vibration of the structure, we will consider these effects in the next chapter when we extend this analysis to 2-D. Next, though, we will discuss the applicability of the beam under axial load theory.

#### **5.4.2 Limits of the Beam under Axial Load Theory**

To further validate the use of the optimal parameter values, the developed model was used to predict the response of the Kapton and PZT structure under multiple tensile loadings varying from 0.6 to 19 N. The developed FE model was able to predict the response of the structure to within 5% accuracy for tensile loads greater than 4 N. At a

tensile load of 19 N, the membrane strip began to visually undergo noticeable deformation. Since such behavior is beyond the anticipated tensile range of the membrane optic, 19 N was established as the upper load limit for the model. A graphic of the errors between the FE model predicted frequencies and the experimentally measured frequencies at multiple tensile loads is shown in Figure 5.12.

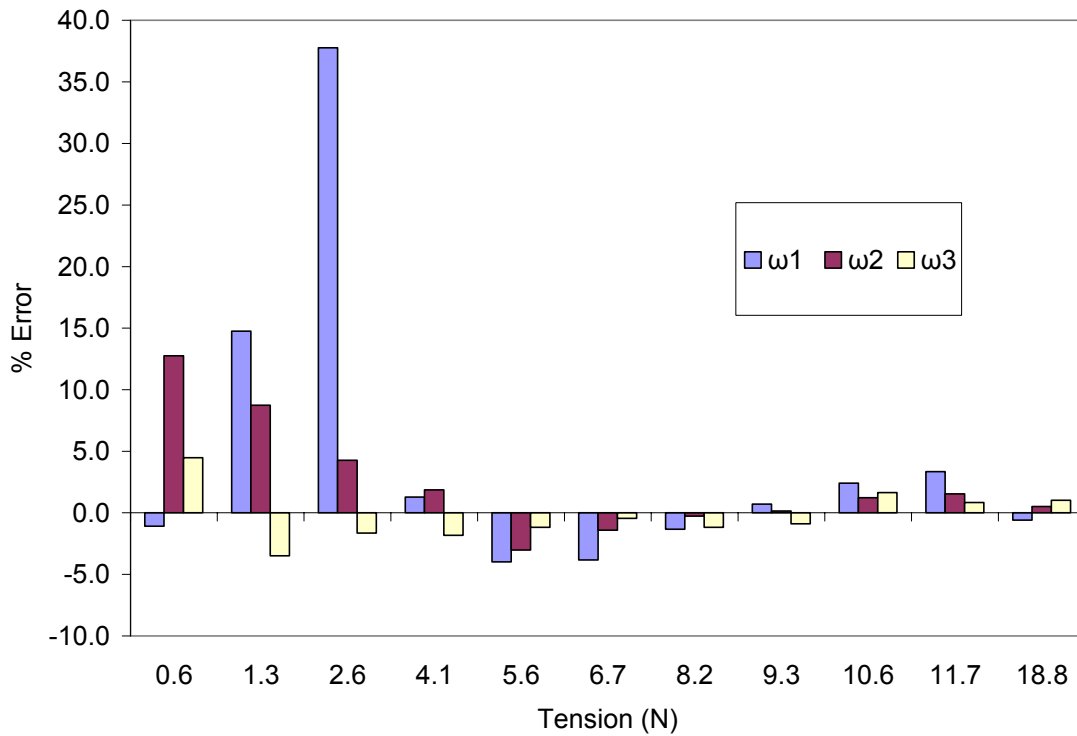


**Figure 5.12.** The error between experimental frequencies and the first three out-of-plane frequencies predicted by the developed FE model at multiple tensile loads.

As shown by Figure 5.12, the developed FE model predicts the first three out-of-plane frequencies of the augmented membrane sample to within 5% accuracy between tensile loading values of 4 N to 19 N. Below 4 N, the model doesn't perform nearly as well, with errors on the order of 10, 15, and even 37% between the measured and the predicted frequency values. Consequently, 4 N is a lower limit on the applicability of the beam under tensile load theory in predicting the response of membrane strips augmented with PZT.

## 5.5 Mass Effects on the System Frequencies

Another important issue to consider is the effect that the PZT mass has on the dynamics of the active membrane strip. Since we have established the validity of the finite element model compared to experimentally measured data, we can use the FE model to understand the effect of bonding larger or smaller PZT bimorphs to the membrane sample. In the simulation, we will keep the mass and length of the membrane strip constant and modify the length of the actuator. For reference, during the experimental work performed earlier in this chapter, the actuator represented 36% of the total system mass. In the simulations, the PZT length was varied such that it represented from 27% of the total system mass to 69% of the total system mass. Figures 5.13, 5.14, and 5.15 demonstrate the behavior of the first three resonant frequencies of the augmented system as the length of the actuator is modified.

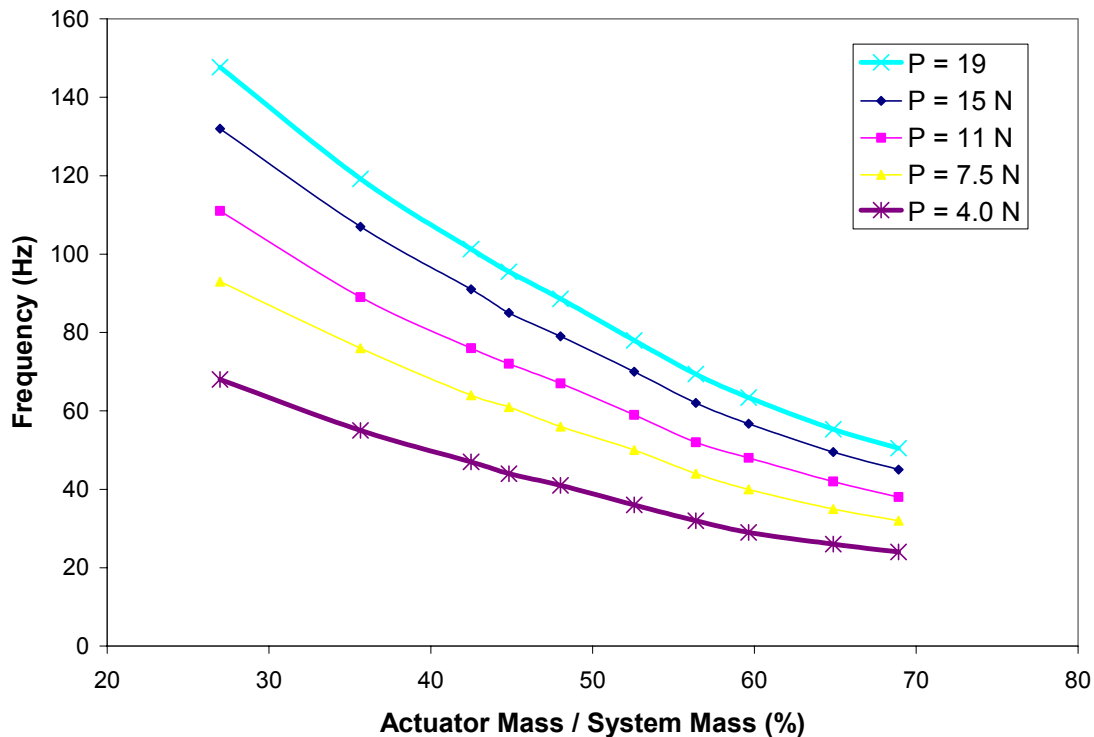


**Figure 5.13.** Adding additional mass to the system via the size of the actuator decreases the first resonant frequency of the combined system.

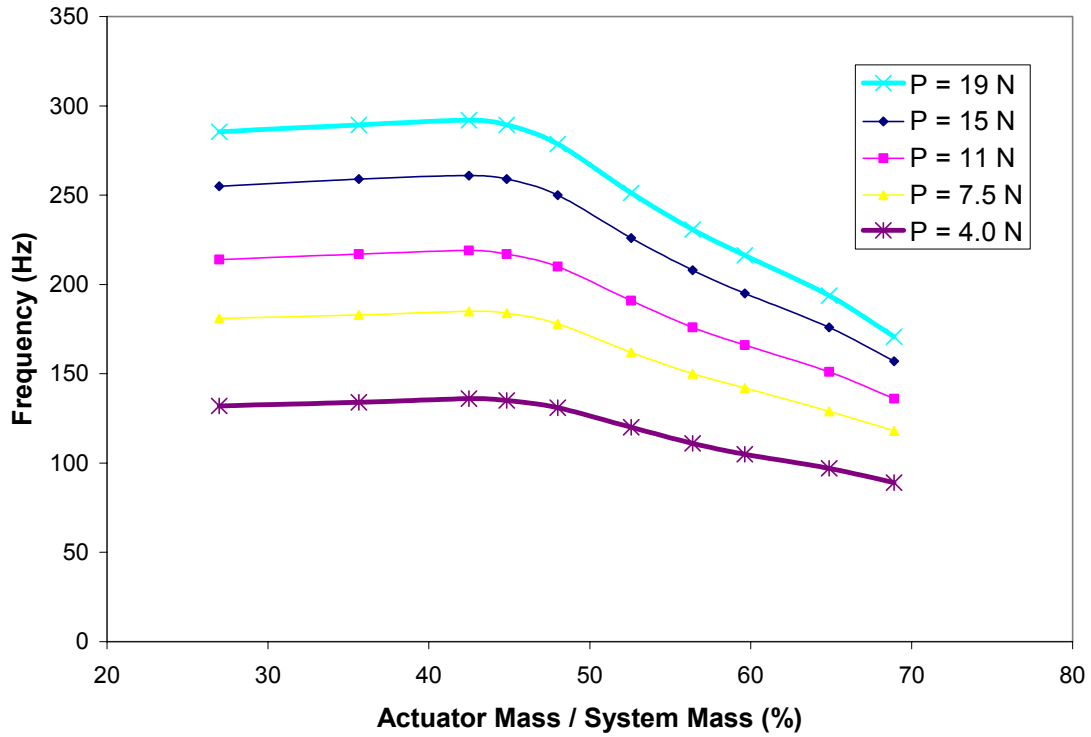


**Figure 5.14.** Adding additional mass to the system via the size of the actuator decreases the second resonant frequency of the combined system, but only after reaching an actuator mass percentage of 45%.

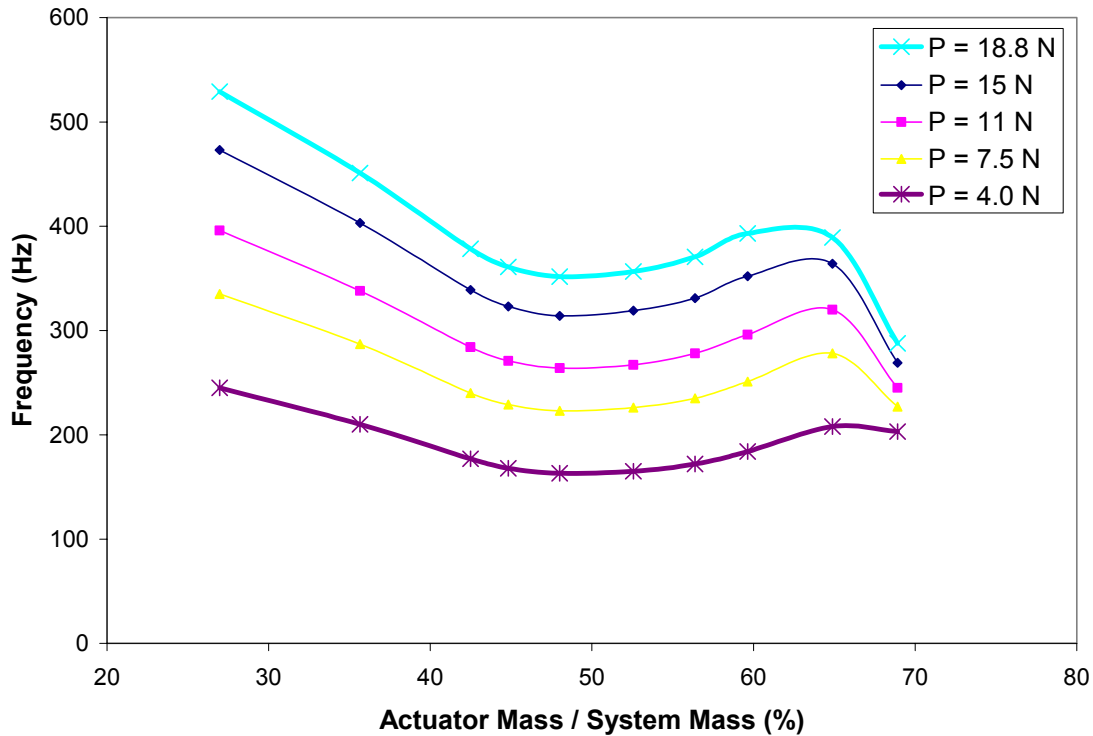


**Figure 5.15.** Adding additional mass to the system via the size of the actuator initially decreases the third resonant frequency of the combined system, but then increases again after reaching an actuator mass percentage of 45%.

Figures 5.13 – 5.15 highlight from a structural design perspective that the addition of significant piezoelectric material mass to the system can significantly degrade the bandwidth of the combined system, which may be detrimental to the optic or radar aperture design. A tradeoff exists between control authority over the structure (increased PZT area on the surface of the optic or radar) and the resulting bandwidth of the system.

Lastly, we wish to investigate the assertion that the out-gassing experienced by the Kapton sample at vacuum is responsible for the frequency shift demonstrated in the experimental results. During the experimental testing under vacuum conditions, the load cell measured an applied tensile load of 14.4 N. At ambient conditions, though, the load cell measured an applied tensile load of 13.5 N. Simulating the response of the membrane – PZT system at each of these loadings produced frequency shifts comparable to the shifts demonstrated experimentally. Therefore, it is concluded that the out-gassing

phenomenon is one of the major contributors to the frequency discrepancies demonstrated experimentally between the vacuum and ambient test data. Another source of discrepancy is a mass loading effect at ambient pressure from the surrounding air (Kukathasan and Pellegrino, 2003). This effect would also decrease the resonant frequencies of the structure. A summary of the simulated and experimental results with regards to out-gassing is given in Table 5.2.

**Table 5.2.** Comparison between experimental and FEM predicted responses of the membrane – PZT system subject to out-gassing at vacuum

Tensile Load (N)	Experimental			FEM		
	14.4	13.5	% Change	14.4	13.5	% Change
$\omega_1$ (Hz)	86	83	3.5	87	84	3.4
$\omega_2$ (Hz)	267	245	8.2	284	274	3.5
$\omega_3$ (Hz)	352	321	8.8	346	334	3.5

## 5.6 Formulation of the LQR Control Problem

Now, we wish to construct a linear quadratic regulator (LQR) controller to use the PZT bimorph as an actuator to eliminate detrimental vibration from the system. The optimal control problem is stated as follows:

Given  $z(0) \in R^{2N}$ , a vector containing the states of the system, choose a control  $u \in L_2(0, \infty; R^m)$  to minimize the cost functional

$$J_N(z(0), u) = \int_0^{\infty} [z(t)^T Q^N z(t) + u(t)^T R u(t)] dt. \quad (5.33)$$

$Q^N$  is a symmetric, non-negative  $2n \times 2n$  matrix, and  $R$  is a scalar value since we only have one control input (the voltage supplied to the PZT bimorph actuator). We can define our  $Q^N$  matrix in the following manner. Following the methodology of Gibson and Adamian (1991), we will define the entries to the  $Q^N$  matrix based on the potential and kinetic energies of the system. We can thereby define

$$Q^N = \begin{bmatrix} Q_1^N & 0 \\ 0 & Q_2^N \end{bmatrix} \quad (5.34)$$

where the potential strain energy of the system is given by

$$Q_1^N = q_1 \left[ \int_0^L [EI(\psi_{xx})_i](\psi_{xx})_j dx + \int_0^L [P(x)(\psi_x)_i](\psi_x)_j dx \right]_{i,j=1}^N \quad (5.35)$$

and the kinetic energy of the system is given by

$$Q_2^N = q_2 \left[ \int_0^L \{\rho A(\psi_i)(\psi_j)\} dx \right]_{i,j=1}^N. \quad (5.36)$$

The terms  $q_1$  and  $q_2$  are weighting terms that can be determined by the control designer. For completeness, the  $R$  matrix for this particular LQR problem is defined as

$$R = [r]. \quad (5.37)$$

The upper and lower diagonal entries of the  $Q^N$  matrix correspond to twice the total energy of the structure (Gibson and Adamian, 1991). The optimal control,  $u_N$ , is given by

$$u_N(t) = -K^N z(t), \quad (5.38)$$

where

$$K^N = R^{-1} [B^N]^T \Pi^N \quad (5.39)$$

and  $\Pi^N$  is the minimal, symmetric, non-negative solution to the Riccati equation

$$\left[A^N\right]^T \Pi^N + \Pi^N A^N - \Pi^N B^N R^{-1} \left[B^N\right]^T \Pi^N + Q^N = 0. \quad (5.40)$$

Implementing this control design with our Kapton—PZT bimorph structure, and choosing

$$\left[q_1 \quad q_2 \quad r\right] = \left[100000 \quad 100000 \quad 0.0001\right], \quad (5.41)$$

we can simulate the closed-loop response of the structure. Figures 5.16 and 5.17 show the open loop and closed-loop response of the structure, respectively.

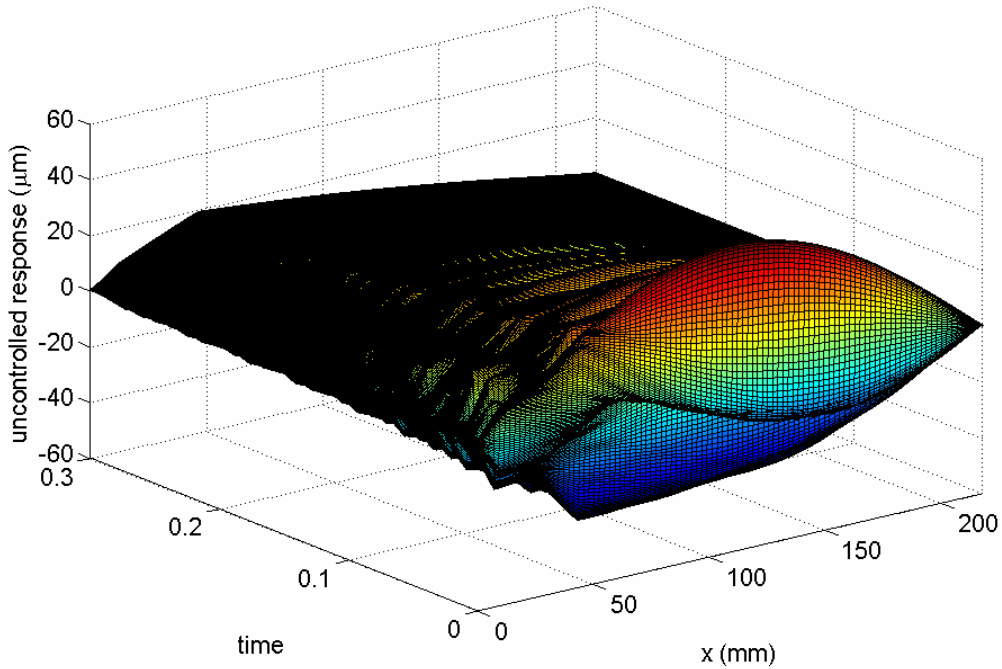


**Figure 5.16.** Simulated open-loop response of the membrane-PZT system subject

to an initial disturbance of  $w(x,0) = \frac{1}{20000} \sin\left(\frac{\pi x}{L_b}\right)$ .

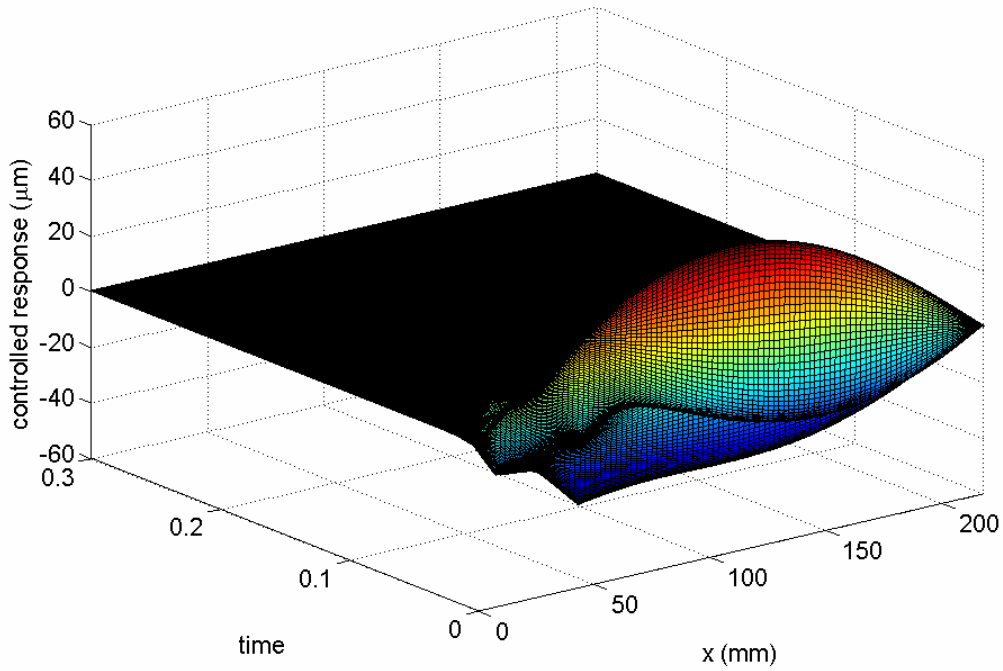


**Figure 5.17.** Simulated closed-loop response of the membrane-PZT system

subject to an initial disturbance of  $w(x,0) = \frac{1}{20000} \sin\left(\frac{\pi x}{L_b}\right)$ .

The controlled response (Figure 5.17) demonstrates excellent elimination of the non-zero initial conditions of the system. With a maximum initial voltage of 9 V, the LQR controller returns the system to a zero state within 0.15 s. The weightings (Equation 5.41) could be tailored to reduce the settling time further (at a consequence of increased control effort), or to relax the settling time requirement (and consequently reduce the required control effort). Such system properties are subject to the mission requirements.

## 5.7 Introduction to Functional Gains

Functional gains are a product of defining the optimal control problem for a distributed parameter system. More specifically, they are kernels of the feedback operator, and they offer insight into actuator or sensor placement (Burns and Hulsing, 2001) based on the choice of control. Some research has already been performed looking at the functional gains of mechanical systems and using the results for intelligent, or informed, actuator and sensor placement within the systems. Tadi (1993) investigated the functional gains for controlling a Mindlin plate, a plate model that includes the effects of transverse shear and rotary inertia. Tadi calculated the functional gains associated with a generic control input, and set up the mathematical framework for demonstrating convergence of both the finite element model and the functional gains using cubic B-splines. In 1998, Tadi (1998) investigated the slewing dynamics of a Timoshenko beam with a tip mass rotating around a fixed hub, and again looked at the functional gains as generated by a finite element model of the system using cubic B-splines. Using a method known as Tessler's scheme, which is based on conforming finite elements (Tessler and Dong, 1981), Tadi analyzed the convergence of the finite element model as the beam's parameters were varied from that of an Euler-Bernoulli beam to that of a Timoshenko beam.

Miller (1998) proposed the idea of using the functional gains of a system as part of a Gaussian quadrature scheme for optimally placing sensors in a system. Miller developed a finite element model of a slewing Euler-Bernoulli beam with tip mass using cubic B-splines, and then computed the optimal gains. From the kernels of the optimal gains, he extracted the functional gains. He then demonstrated that the functional gains can be used as the weighing functions in a Gaussian quadrature formula, and the resulting nodes of the Gaussian quadrature correspond to optimal locations for sensor placement. He demonstrated his analysis through numerical studies. Burns and Hulsing (2001) presented different numerical methods for calculating the functional gains, focusing on issues that arise when the system size increases tremendously for 2-D and 3-D problems.

For our Kapton substrate system, we have already defined our  $Q^N$  and  $R$  matrices for the LQR control problem. Following the notation of Gibson and Adamian (1991), the

functional gains  $k_s$  and  $k_v$ , corresponding to the strain energy and kinetic energy of our system, are the kernel functions of our approximation to the optimal control, namely

$$u^N(t) = - \langle k_s^N, z^N(t) \rangle - \langle k_v^N, \dot{z}^N(t) \rangle, \quad (5.42)$$

where, as defined previously, the notation  $\langle f, g \rangle$  implies the inner product of the functions  $f$  and  $g$ . From our definition of the optimal control,  $u(t)$ , as stated in Equation 5.38, and combining that with Equation 5.42, we have

$$-K^N z(t) = - \begin{bmatrix} k_s^N & k_v^N \end{bmatrix} \begin{bmatrix} Q_1^N & 0 \\ 0 & Q_2^N \end{bmatrix} z(t), \quad (5.43)$$

which can also be written as

$$-K^N z(t) = - \begin{bmatrix} k_{gains}^N \end{bmatrix} [Q] z(t). \quad (5.44)$$

Since, by definition,  $Q$  is symmetric and non-negative, we can take its inverse and consequently solve for the functional gains. Doing so, we get

$$\begin{bmatrix} k_{gains}^N \end{bmatrix}^T = [Q]^{-1} [K^N]^T. \quad (5.45)$$

From our previously defined entries for the matrix  $Q$ , we can define the functional gains as

$$k_s^N = [Q_1^N]^{-1} [K^N]^T \quad (5.46)$$

and

$$k_v^N = [Q_2^N]^{-1} [K^N]^T. \quad (5.47)$$

Having defined our functional gains, we now wish to plot them for the Kapton substrate problem. The functional gains for the active Kapton system are shown in Figures 5.18 and 5.19. As a convenient consequence of defining and plotting the functional gains, we can also further demonstrate convergence of the finite element model in stepping from 128 elements to 256 elements. This convergence is demonstrated in both figures.

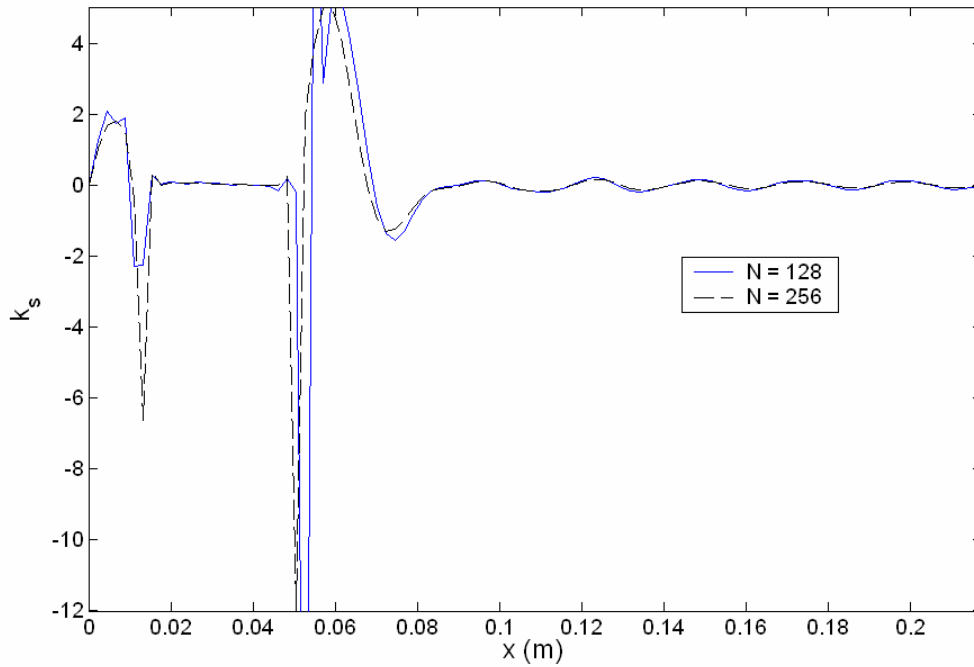


**Figure 5.18.** The strain functional gain for the active Kapton system demonstrates model convergence and can be used for sensor placement.

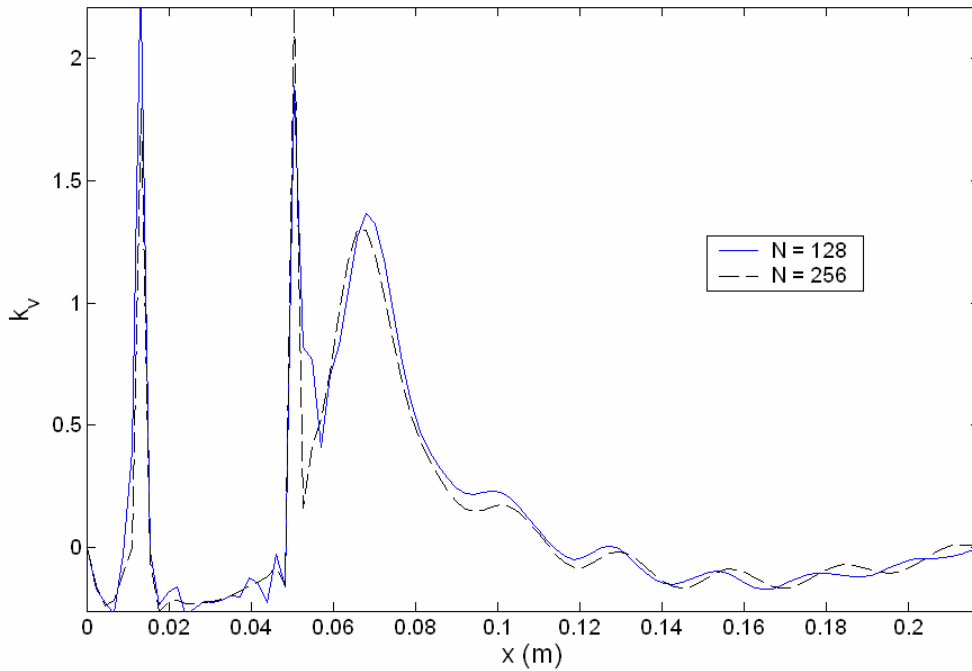


**Figure 5.19.** The velocity functional gain for the active Kapton system demonstrates model convergence and can be used for sensor placement.

As suggested by Miller (1998), the functional gain plots in Figures 5.18 and 5.19 can be used to help determine where the optimal locations for strain and velocity measurements should be taken. In the LQR control problem formulation, it has been assumed that full-state feedback is possible. In reality, such a data acquisition is infeasible to implement, and control engineers need to design optimal controllers based on discrete sensor measurements. The portions of the strain and velocity functional gain plots that take on maximum, absolute value are the locations where discrete sensors (i.e. strain gages and possibly a laser vibrometer to measure the local velocity of the structure) should be placed.

To simulate the validity of Miller's (1998) assertion, we will assume that the optimal control signal can be reconstructed based on the average velocity and strain measurements taken from the structure in real time. To simulate this, we will discretize the functional gains (Figures 5.18 and 5.19) based on the locations of maximum

functional gain amplitudes. Figures 5.20 and 5.21 demonstrate the proposed discretization.

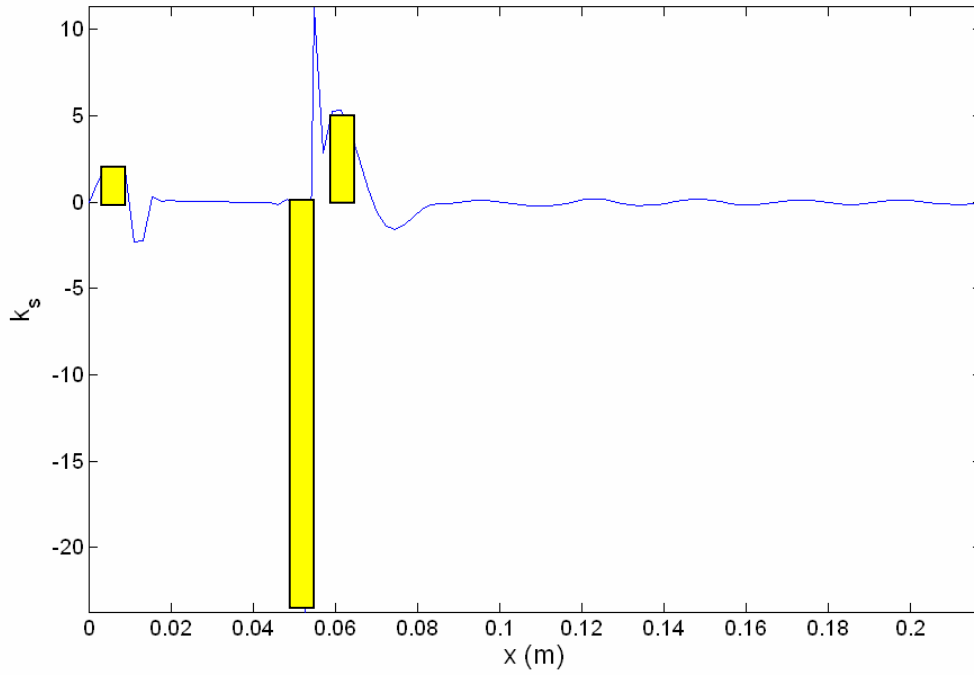


**Figure 5.20.** Proposed discretization of the strain functional gain based on three strain measurement locations.

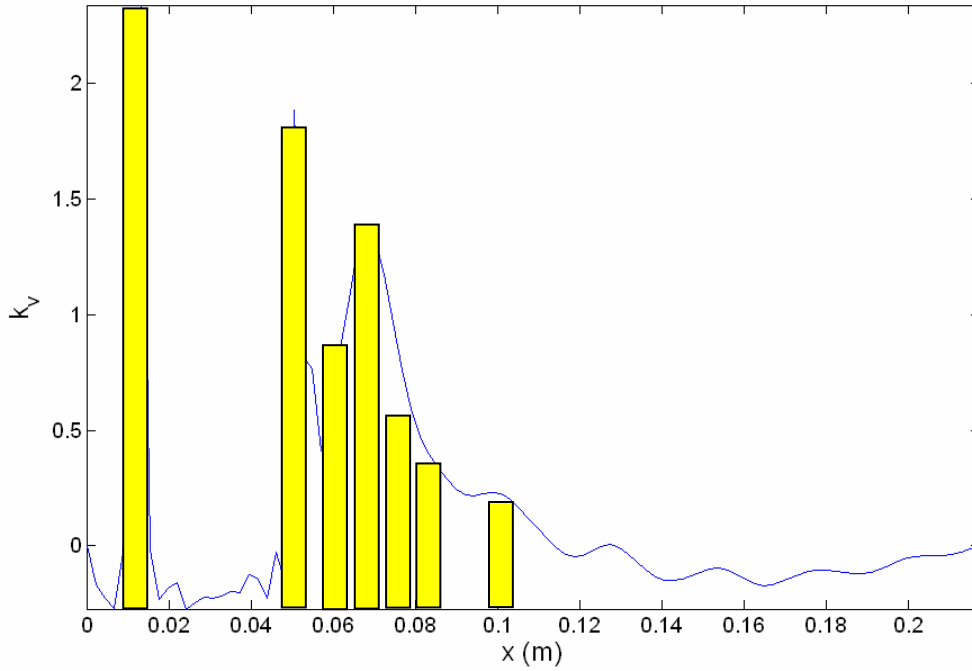


**Figure 5.21.** Proposed discretization of the velocity functional gain based on seven velocity measurement locations.

As stated in Equation 5.42, the optimal control, based on our finite element formulation, is given by

$$u^N(t) = -\langle k_s^N, z^N(t) \rangle - \langle k_v^N, \dot{z}^N(t) \rangle. \quad (5.48)$$

Equation 5.48 is exact in the sense that it is the finite element approximation to the true optimal control signal for the real system. Based on Miller's (1998) work, we can rewrite Equation 5.48 as

$$u^N(t) = -\sum_i (k_v^N)_i v_i(t) - \sum_i (k_s^N)_i \varepsilon_i(t), \quad (5.49)$$

where the average velocity measured by the laser vibrometer is given by

$$v_i = \frac{1}{y_2 - y_1} \int_{y_1}^{y_2} v(t) \phi(x) dx, \quad (5.50)$$

and the average strain measurement is given by

$$\varepsilon_i = \frac{1}{s_2 - s_1} \int_{s_1}^{s_2} K_b d(t) \phi''(x) dx. \quad (5.51)$$

In Equations 5.49, 5.50, and 5.51,  $y_1$ ,  $y_2$ ,  $s_1$ , and  $s_2$  refer to the left and right spatial locations of the laser vibrometer dot and the strain gages, respectively. Now we can reconstruct the optimal control signal based on our discretized measurements. Figure 5.22 simulates the finite element-generated optimal control signal (as given by Equation 5.48) and the approximated optimal control based on the functional gain-generated control signal (as given by Equation 5.49 using three strain measurements and seven velocity measurements according to the discretizations of Figures 5.20 and 5.21).

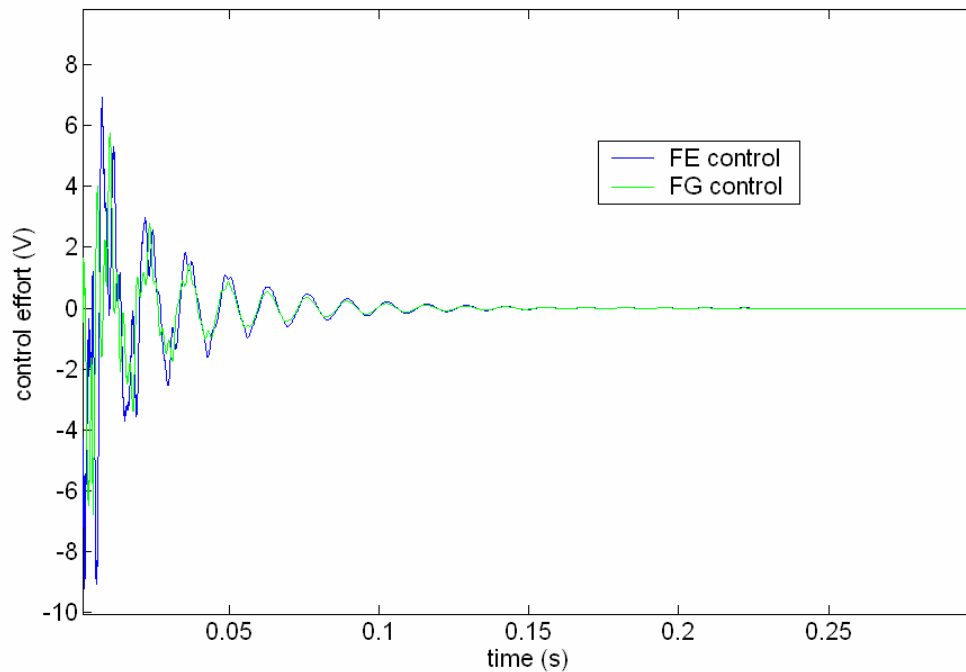


**Figure 5.22.** The optimal control signal can be reconstructed using the generated functional gains of the system. Shown here is the optimal control signal based on the finite element model (FE) and the approximated functional gain model (FG).

Figure 5.22 highlights the benefits of our distributed system and control problem modeling. A different method of attacking the control problem would have been to design an LQG controller (i.e. observer) based on the use of strain gages and velocity feedback. In both the formulation of the functional gain problem and the formulation of an LQG controller, the goal is to design an effective controller based on limited state feedback. The formulation of the functional gain problem, however, offers additional insight as to where particular sensors should be placed within the system based on the physics governing the dynamics. Traditionally, observer-based design begins with set locations determined for each sensor. As the functional gain analysis has demonstrated, sensor placement can be optimized rather quickly by analyzing the functional gains of the system. Consequently, the additional effort used in computing the functional gains of the distributed parameter system is immediately rewarded in that sensors can be placed ideally without much trial-and-error experimental work. And if the location of actuators within the system is another design parameter, then formulation of the dual problem for the infinite-dimensional optimal observer would produce a second set of functional gains that could be used for intelligent placement of actuators, as well.

## **5.8 Chapter Summary**

In summary, the weak form governing the dynamics of a pinned-pinned Euler-Bernoulli beam under axial loading has been developed to model an integrated piezoelectric bimorph and Kapton membrane substrate strip sample. The integrated system was modeled using finite element cubic B-splines, and validated through extensive testing of a PZT-Kapton sample in the bandwidth of 0 – 500 Hz. Excellent agreement was found between the experimental data and the finite element model. The model correlated well with the experimental data between applied tensile loads of 4 N to 19 N. At 19 N, the Kapton began to experience visual deformation, and consequently was established as the upper limit on the model, as the structure would begin to behave non-linearly in the plastic region. Below 4 N, the agreement between the finite element model and the experimental test data was much less desirable, with errors greater than 15% between the two.

The phenomenon known as out-gassing, which has been documented to occur in Kapton, was shown to attribute to discrepancies in test data between vacuum and ambient tests. The loss of material mass due to out-gassing caused an increase in the tensile loading applied under ambient conditions by 5%, and consequently the frequencies of the structure increased by up to 8% between the ambient and vacuum cases. This assertion was demonstrated by modeling the change in tension applied to the Kapton material in the finite element model and examining the effect on the frequencies of the system. The change in tensile loading induced by the outgassing phenomenon attributed for up to 4% frequency shifts in the simulated response. The further discrepancy from ambient to vacuum conditions in the experimental data is attributed to air mass loading at ambient conditions.

The linear quadratic regulator (LQR) problem was formulated to simulate how the piezoelectric bimorph could be used to reduce and eliminate detrimental vibration of the membrane. By formulating the LQR problem, we are also able to calculate the functional gains of the system. Since the dominant states are strain and velocity of the structure, the strain and velocity functional gains were computed and plotted. The benefit of plotting the functional gains is that they can be used to demonstrate model convergence and to show spatially the optimal locations to measure state information from the system. Since full-state feedback is hardly ever an option in most control designs, the functional gains can be used as a tool for placing sensors intelligently within a system.

Now that we have established the validity of using beam under axial loading theory for our closed-loop system model, the next chapter will focus on extending these results to 2-D via thin plate theory.